

## 2 **In-situ calibration of the single-photoelectron** 3 **charge response of the IceCube photomultipliers**

---

**IceCube author list to be inserted... E-mail:** `analyses@icecube.wisc.edu`

4 **ABSTRACT:** This article outlines the in-situ calibration of the single-photoelectron charge distributions for each of the Hamamatsu Photonics R7081-02 (MOD) photomultipliers in the IceCube Neutrino Observatory. The accurate characterization of the individual PMT charge distributions is important for event reconstruction and calibration. We discuss the single photoelectron identification procedure and how we extract the single-photoelectron charge distribution using a deconvolution of the multiple photoelectron charge distribution, and we examine various correlations between the shape of the single-photoelectron charge distribution and various hardware components. The time dependence of the individual PMT charge distributions is also investigated.

5 **KEYWORDS:** IceCube, single photoelectron, charge distribution, PMT.

---

## 7 Contents

8	<b>1. Introduction</b>	<b>1</b>
9	1.1 Single-photoelectron charge distributions	3
10	1.2 IceCube datasets and software definitions	5
11	<b>2. Extracting the SPE templates</b>	<b>6</b>
12	2.1 Single photoelectron pulse selection	6
13	2.2 Characterizing the low-charge region	8
14	2.3 Fitting procedure	9
15	2.4 SPE template fit results	10
16	<b>3. Discussion</b>	<b>10</b>
17	3.1 Correlations between fit parameters and DOM hardware differences	10
18	3.2 Fitting parameters variation over time	13
19	3.3 Quantifying observable changes when modifying the PMT charge distributions	13
20	3.3.1 Model comparison	14
21	3.4 SPE templates in simulation	15
22	3.5 SPE templates for calibration	16
23	<b>4. Conclusion</b>	<b>16</b>

---

## 25 1. Introduction

26 The IceCube Neutrino Observatory [1, 2] is a cubic-kilometer-sized array of 5,160 photomultiplier  
 27 tubes (PMTs) buried in the Antarctic ice sheet, designed to observe high-energy neutrinos interact-  
 28 ing with the ice [3]. In 2011, the IceCube Collaboration completed the installation of 86 vertical  
 29 *strings* of PMT modules, eight of which were arranged in a denser configuration known as the  
 30 DeepCore sub-array located in the clearest ice near the bottom of the detector [4]. Each string in  
 31 IceCube contains 60 digital optical modules (DOMs), which contain a single PMT each, as well as  
 32 all required electronics [5]. The primary 78 strings (excluding DeepCore) are spaced 125 m apart  
 33 in a hexagonal grid, with the DOMs extending from 1450 m to 2450 m below the surface of the ice  
 34 sheet. The additional DeepCore strings (79-86) are positioned between the centermost strings in  
 35 the detector, reducing the horizontal DOM-to-DOM distance in this region to 42 m and 72 m.

36 Each DOM consists of a 0.5" thick spherical glass pressure vessel that houses a single down-  
 37 facing 10" PMT from Hamamatsu Photonics. The PMT is coupled to the glass housing with optical  
 38 gel and is surrounded by a wire mesh of mu metal to reduce the effect of the Earth's ambient  
 39 magnetic field. The glass housing is transparent to wavelengths 350 nm and above [6].

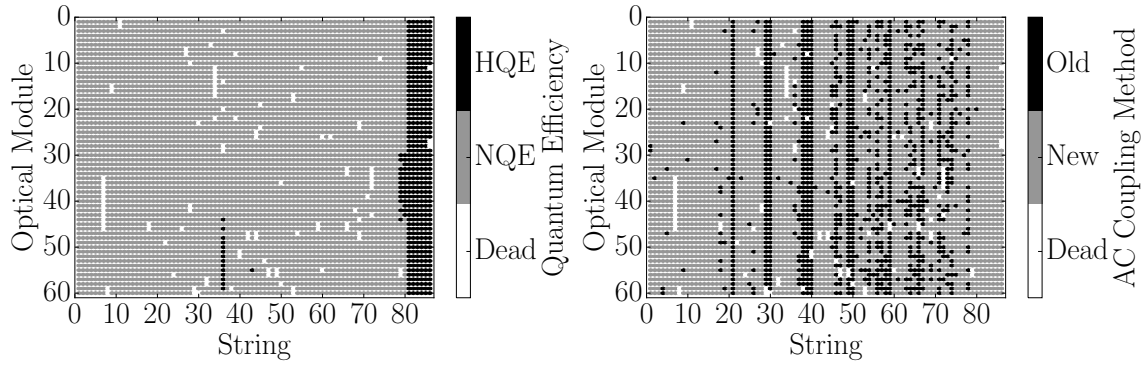


**Figure 1.** Left: A mapping of the HQE (black) and NQE DOMs (gray). Right: The version of AC coupling, old toroids (black) and new toroids (gray). DOMs that have been removed from service are shown in white.

40 Of the 5160 DOMs, 4762 house a R7081-02 Hamamatsu Photonics PMT [7], specified for  
 41 wavelengths ranging from 300 nm to 650 nm, with peak quantum efficiency of 25% near 390 nm.  
 42 These are classified as Standard Quantum Efficiency (NQE) DOMs. The remaining 398 DOMs are  
 43 equipped with the Hamamatsu R7081-02MOD PMTs, which, having a peak quantum efficiency of  
 44 34% near 390 nm (36% higher efficiency than the NQE DOMs), are classified as High Quantum  
 45 Efficiency (HQE) DOMs [4]. These DOMs are primarily located in DeepCore and on strings 36  
 46 and 43, as shown in the left side of Fig. 1.

47 The R7081-02 and R7081-02MOD PMTs have 10 dynode stages and are operated with a gain  
 48 of  $10^7$  and high voltage around 1200 V. A typical amplified single photoelectron will generate a  
 49  $\sim 6$  mV peak voltage at the input to the front-end amplifiers. The PMTs operate with the anodes  
 50 at high voltage and the signal is AC coupled to the front-end amplifiers. There are two versions  
 51 of AC coupling in the detectors, both of which use custom-designed wideband bifilar wound 1:1  
 52 toroidal transformers<sup>1</sup>. The DOM-specific AC-coupling versions, new and old toroids, are shown  
 53 on the right side of Fig. 1. The DOMs with the old toroids were designed with an impedance of  
 54  $43 \Omega$ , while the new toroids are  $50 \Omega$  [8]. All HQE DOMs are instrumented with the new toroids.

55 IceCube relies on two observables per DOM to reconstruct events: the total number of detected  
 56 photons and their timing distribution. Both the timing and the number of photons are extracted from  
 57 the digitized waveforms. This is accomplished by deconvolving the waveforms into a series of  
 58 scaled single photoelectron pulses (so-called pulse series) and the integral of the individual pulses  
 59 (divided by the load resistance) defines the observed charge. It will often be expressed in units of  
 60 PE, or photoelectrons, which further divides the measured charge by the charge of a single electron  
 61 times the nominal gain ( $10^7$ ). Accurate characterization of the individual PMT charge distributions  
 62 is crucial for calibration and event reconstructions relying on charge information. The charge  
 63 distribution can also be used to assess long-term detector performance and identify discrepancies  
 64 between data and Monte Carlo. It is therefore critically important to accurately measure the single-

<sup>1</sup>Conventional AC-coupling high-voltage ceramic capacitors can produce noise from leakage currents and impractical requirements on the capacitors in order to meet the signal droop and undershoot requirements. The toroidal transformer effectively acts as a high-pass filter with good signal fidelity at high frequencies. It also provides higher reliability than capacitive coupling and reduces the stored energy, which might cause damage if there is HV discharge in the system [6]. However, the toroidal-transformer AC coupling also introduces signal droop and undershoot.

65 photoelectron (SPE) charge distribution in order to understand the IceCube detector behavior.

66 When one or more photons produce a voltage at the anode sufficient to trigger the onboard  
67 discriminator (set via a DAC to approximately 1.3 mV, or equivalently to 0.25 PE), the signal ac-  
68 quisition process is triggered. The signal is fed into four parallel input channels. Three of the  
69 channels pass first through a 75 ns delay loop in order to capture the leading edge of the pulse and  
70 then into three high-speed (300 MSPS for 128 samples) 10-bit waveform digitizers (Analog Tran-  
71 sient Waveform Digitizer, ATWD), each of which has a different level of amplification:  $15.7 \pm 0.6$ ,  
72  $1.79 \pm 0.06$ , and  $0.21 \pm 0.01$  [8]. There are also three extra ATWDs on board each DOM: one is  
73 used for calibration and the other two operate in a ping-pong fashion to remove dead time associ-  
74 ated with the readout. The signal to the fourth channel is first shaped and amplified and then fed  
75 into a 10-bit fast analog-to-digital converter (fADC) operating at a sampling speed of 40 MSPS.  
76 Further detail regarding the description of the DOM electronics can be found in Refs. [5, 9].

77 This article discusses the accurate determination of how individual DOMs collect charge in  
78 order to improve calibration and the detector description as used in the IceCube Monte Carlo sim-  
79 ulation. It describes the procedure for determining the PMT’s gain characteristics as seen in the  
80 SPE charge distributions using in-situ data from the IceCube detectors. The SPE charge distribu-  
81 tion refers to the measured charge probability density function of the individual DOMs generated  
82 by the amplification of a pure sample of single photoelectrons. The extraction of the SPE charge  
83 distribution was recently made possible with the development of two pieces of software:

- 84 1. A specially-designed unbiased pulse selection was developed to reduce the multiple photo-  
85 electron (MPE) contamination while accounting for physical phenomena (e.g., late pulses,  
86 afterpulses, pre-pulses, and baseline shifts) and software-related effects (e.g., pulse splitting).  
87 This is further described in Sec. 2.1.
- 88 2. A fitting procedure was developed that separates the remaining MPE contamination from the  
89 SPE charge distribution by deconvolving the measured charged distribution. This is further  
90 described in Sec. 2.3.

91 By using in-situ data to determine the SPE charge distributions, we accurately represent the  
92 individual PMT response as a function of time, environmental conditions, software version, and  
93 hardware differences, and we sample photons uniformly over the surface of the photocathode. This  
94 is beneficial since it also allows us to inspect the stability and long-term behavior of the individual  
95 DOMs, verify previous calibration, and correlate features and environment to DOM behavior.

## 96 1.1 Single-photoelectron charge distributions

97 In an idealized scenario, a single photon produces a single photoelectron, which is then amplified by  
98 a known amount and the measured charge corresponds to 1 PE. However, there are many physical  
99 processes that create structure in the measured charge distributions. For example:

- 100 • **Statistical fluctuation due to cascade multiplication** [10]. At every stage of dynode am-  
101 plification, there is a stochastic spread in the number of emitted electrons that make it to the  
102 next dynode. This in turn causes a spread in the measured charge after the gain stage of the  
103 PMT.

- 104 • **Photoelectron trajectory.** Some electrons may deviate from the favorable trajectory, reduc-  
 105 ing the number of secondaries produced at a dynode or the efficiency to collect them on the  
 106 following dynode. This can occur at any stage, but it has the largest effect on the multipli-  
 107 cation at the first dynode [11]. The trajectory of a photoelectron striking the first dynode  
 108 will depend on many things, including where on the photocathode it was emitted, the unifor-  
 109 mity of the electric field, the size and shape of the dynodes [10], and the ambient magnetic  
 110 field [12, 13].
  
- 111 • **Late or delayed pulses.** A photoelectron can elastically or inelastically scatter off the first  
 112 dynode. The scattered electron can then be re-accelerated to the dynode, creating a second  
 113 pulse. The difference in time between the initial pulse and the re-accelerated pulse in the  
 114 R7081-02 PMT was previously measured to be up to 70 ns [6, 14]. The two sub-pulses have  
 115 lower charges, but the sum of the two tends to add up to the original charge. Collecting either  
 116 the initial pulse or the late pulse will result in the charge being reconstructed in the low-PE  
 117 region [15].
  
- 118 • **Afterpulses.** When a photoelectron or the secondary electrons produced during the electron  
 119 cascade gain sufficient energy to ionize residual gas in the PMT, the positively charged ion-  
 120 ized gas will be accelerated in the electric field towards the photocathode. Upon impact with  
 121 the photocathode, electrons can be again released from the photocathode, creating what is  
 122 called an afterpulse. For the R7081-02 PMTs, the timescale for afterpulses was measured  
 123 to occur from 0.3 to 11  $\mu$ s after the initial pulse, with the first prominent afterpulse peak  
 124 occurring at approximately 600 ns [6]. The spread in the afterpulse time is dependent on  
 125 the position of photocathode, the charge-to-mass ratio of the ion produced, and the electric  
 126 potential distribution [16], whereas the size of the afterpulse is related to the momentum and  
 127 species of the ionized gas and composition of the photocathode [17].
  
- 128 • **Pre-pulses.** If an incident photon passes through the photocathode without interaction and  
 129 strikes one of the dynodes, it can eject an electron that is only amplified by the subsequent  
 130 stages, resulting in a lower measured charge (lower by a factor of approximately 25). For  
 131 the IceCube PMTs, the prepulses have been found to arrive approximately 30 ns before the  
 132 signal from other photoelectrons from the photocathode [6].
  
- 133 • **MPE contamination.** When multiple photoelectrons arrive at the first dynodes within sev-  
 134 eral nanoseconds of each other, they can be reconstructed by the software as a single, MPE  
 135 pulse.
  
- 136 • **Electronic noise.** This refers to the fluctuations in the analog-to-digital converters (ATWDs  
 137 and FADC) and ringing that arises from the electronics.

138 Beyond the physical phenomena above that modify the measured charge distribution, there is  
 139 also a lower limit on the smallest charge that can be extracted. For IceCube, the discriminator limits  
 140 the trigger pulse to be above approximately 0.25 PE, and subsequent pulses in the readout time  
 141 window are subject to a software-defined threshold. The software threshold was set conservatively

142 to avoid extracting pulses that originated from electronic noise. This threshold can be modified to  
 143 gain access to lower charge pulses and will be discussed in Sec. 2.2.

144 The standard SPE charge distribution model used by the IceCube Collaboration, known as the  
 145 TA0003 distribution [6], represented the above effects as the sum of an exponential plus a Gaus-  
 146 sian. The exponential component represented charge of poorly amplified pulses and the Gaussian  
 147 represented the spread in statistical fluctuations due to the cascade multiplication. The TA0003  
 148 distribution was previously used to describe all the PMTs in the IceCube detectors.

149 Recently, IceCube has performed several lab measurements using the R7081-02 PMTs with in-  
 150 time laser pulses, demonstrating that the in-time charge distribution includes a steeply falling low-  
 151 charge component below the discriminator threshold. To account for this, a new functional form  
 152 including a second exponential was introduced. This form of the charge distribution  $f(q)_{SPE} =$   
 153  $\text{Exp}_1 + \text{Exp}_2 + \text{Gaussian}$ , is referred to as the *SPE template* in this article. Explicitly, it is:

$$f(q)_{SPE} = E_1 e^{-q/w_1} + E_2 e^{-q/w_2} + N e^{-\frac{(q-\mu)^2}{2\sigma^2}}, \quad (1.1)$$

154 where  $q$  represents the measured charge;  $E_1$ ,  $E_2$ , and  $N$  represent normalization factors of each  
 155 components;  $w_1$  and  $w_2$  are the exponential decay widths; and  $\mu$ ,  $\sigma$  are the Gaussian mean and  
 156 width, respectively. This is the assumed functional shape of the SPE charge distributions and the  
 157 components of Eq. 1.1 are determined in this article for all in-ice DOMs. IceCube defines 1 PE as  
 158 the location of the Gaussian mean ( $\mu$ ) and calibrates the gain on the individual PMTs during the  
 159 start of each season to meet this definition. The choice of where we define 1 PE is arbitrary, since  
 160 linearity between the total charge collected and the number of incident photons is satisfied up to  
 161 and beyond  $\sim 2$  V [8]. This is because the average of the distribution is a set fraction of the Gaussian  
 162 mean and the mean of a  $N$ -fold convolution is the sum of means. Any bias in the total observed  
 163 charge can be absorbed into an efficiency term, such as the quantum efficiency.

## 164 1.2 IceCube datasets and software definitions

165 The largest contribution to the IceCube trigger rate comes from downgoing muons produced in  
 166 cosmic ray induced showers [18]. Cosmic ray muons stopping in the detector cause the individ-  
 167 ual trigger rate to decrease at lower depths. Further, climate variations during the formation of  
 168 the ice sheet caused depth-dependent variations in the optical properties of the ice. The optical  
 169 properties also affect the trigger rate; in particular, the “dust layer” from 2100 to 2200 m below the  
 170 surface (optical modules 32 to 38 in the IceCube detector) is a region in the ice with relatively large  
 171 scattering and absorption coefficients [19].

172 An induced signal in the PMT that passes through the AC coupling toroid located on the  
 173 base of the PMT is compared to a discriminator threshold. If a DOM and its nearest or next to  
 174 nearest neighbor observe a discriminator threshold crossing within a set time window, a *hard local*  
 175 *coincidence* (HLC) is initiated and the corresponding waveforms are sampled 128 times and read  
 176 out on the three ATWDs.

177 After waveform digitization, there is a correction applied to remove the measured DC base-  
 178 line offset. The signal droop and undershoot introduced by the toroidal transformer AC coupling  
 179 is compensated for in software during waveform calibration, by adding the expected temperature-  
 180 dependent reaction voltage of the undershoot to the calibrated waveform. If the undershoot voltage

181 drops below 0 ADC counts, the ADC values are zeroed and then compensated for once the wave-  
182 form is above the minimum ADC input. Scaled single photoelectron pulse shapes (that take into  
183 account the version of the AC coupling) are then fit to the waveforms using software referred to  
184 as WaveDeform (waveform unfolding process), which determines the individual pulse time stamps  
185 and charges and populates a pulse series [20].

186 The pulse series used in this analysis come from two datasets provided by IceCube:

- 187 1. The **MinBias dataset**. This dataset records the full waveform readout of randomly-triggered  
188 HLC events at a rate that corresponds on average to 1/1000 events. The largest contribution  
189 to the IceCube trigger rate comes from downgoing muons produced in cosmic-ray-induced  
190 showers [18] and therefore is the largest signal component in this dataset. These muons tend  
191 to have small energies when they reach the detector, thus they produce minimal MPE con-  
192 tamination. The full waveform of these events allows us to extract the raw information about  
193 the individual pulses. This will be used to measure the individual PMT charge distributions.
- 194 2. The **BeaconLaunch dataset**. This is a forced triggered filter that is typically used to mon-  
195 itor the individual DOM baseline. It includes the full ATWD-window waveform readout.  
196 Since this dataset is forced-triggered, the majority of these waveforms represent baseline  
197 fluctuations with minimal contamination from the occasional coincidental pulse that makes  
198 it into the readout window. This dataset will be used to examine the noise contribution to  
199 the charge distributions. Note: when using this dataset, the weight of every pulse is multi-  
200 plied by a factor of 28.4 to account for the livetime difference between the MinBias dataset  
201 and the BeaconLaunch dataset. Weight, in this context, refers to the number of photons in  
202 the MinBias dataset proportional to one photon in the BeaconLaunch dataset for which both  
203 datasets have the same equivalent livetime.

204 This analysis uses the full MinBias and BeaconLaunch datasets from IceCube seasons 2011  
205 to 2016 (subsequently referred to as IC86.2011 to IC86.2016). Seasons in IceCube typically start  
206 in June of the labeled year and end approximately one year later. Calibration is performed at the  
207 beginning of each season.

## 208 2. Extracting the SPE templates

### 209 2.1 Single photoelectron pulse selection

210 The pulse selection is the method used to extract candidate, unbiased, single photoelectron pulses  
211 from data while minimizing the MPE contamination. It avoids collecting afterpulses, rejects late  
212 pulses from the trigger, reassembles late pulses, accounts for the discriminator threshold, reduces  
213 the effect of droop and baseline undershoot, and gives sufficient statistics to perform a season-to-  
214 season measurement. An illustrative diagram of the pulse selection is shown in the left side of  
215 Fig. 2, while a description of the procedure is detailed below.

216 We restrict the pulse selection to only extract information from waveforms in which the trigger  
217 pulse does not exceed 10 mV and no subsequent part of the waveform exceeds 20 mV. This reduces  
218 the effect of the baseline undershoot due to the AC coupling or other artifacts from large pulses.

219 In order to trigger a DOM, the input to the front-end amplifiers must exceed the discriminator  
 220 threshold. To avoid the selection bias of the discriminator trigger, we ignore the trigger pulse as  
 221 well as the entire first 100 ns of the time window. Ignoring the first 100 ns has the added benefit  
 222 of also removing late pulses that could be attributed to the triggering pulse. To ensure we are not  
 223 accepting afterpulses into the selection, we also enforce the constraint that the pulse of interest  
 224 (POI) is within the first 375 ns of the ATWD time window. This also allows us to examine the  
 225 waveform up to 50 ns after the POI. In the vicinity of the POI, we check that WaveDeform did not  
 226 reconstruct any pulses up to 50 ns prior to the POI, or 100 to 150 ns after the POI (the light gray  
 227 region of Fig. 2 (left)). This latter constraint is to reduce the probability of accidentally splitting a  
 228 late pulse in the summation window.

229 If a pulse is reconstructed between 100 and 375 ns after the time window is opened and the  
 230 voltage criteria are met, it is accepted as a candidate photoelectron and several checks are performed  
 231 on the waveform prior to and after the pulse. The first check is to ensure that the waveform is near  
 232 the baseline just before the rising edge of the POI. This is accomplished by ensuring that the  
 233 waveform does not exceed 1 mV, 50 to 20 ns prior to the POI, and eliminates cases where the POI  
 234 is a late pulse. We also ensure the waveform returns to the baseline by checking that no ADC  
 235 measurement exceeds 1 mV, 100 to 150 ns after the POI. These constraints are illustrated as the  
 236 horizontal red dotted lines and black arrows in the left side of Fig. 2.

237 If all the above criteria are met, we sum the reconstructed charges from the POI time, given by  
 238 WaveDeform, to +100 ns (the dark gray area in Fig. 2 (left)). This ensures that any nearby pulses  
 239 are either fully separated or fully added. WaveDeform may occasionally split an SPE pulse into

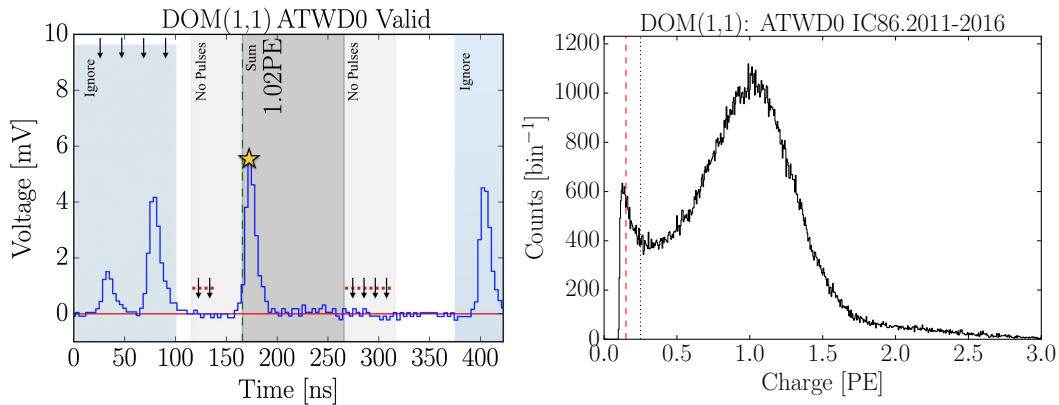


**Figure 2.** Left: An illustrative diagram of the pulse selection criteria for selecting a high-purity and unbiased sample of single photoelectrons. The digitized ATWD waveform is shown in blue. The pulse of interest is identified with a yellow star. This example waveform was triggered by a small pulse at 25 ns (recall that the delay board allows us to examine the waveform just prior to the trigger pulse), followed by a potential late pulse at 70 ns. At 400 ns, we see a pulse in the region susceptible to afterpulses. Waveform voltage checks are illustrated with arrows, and various time windows described in the text are drawn with semiopaque regions. The POI is reported to have a charge of 1.02 PE, given by WaveDeform, and would pass the pulse selection criteria. Right: The collected charges from string 1, optical module 1 (DOM 1,1), from the MinBias dataset collected from IC86.2011 to IC86.2016 that pass the pulse selection. The discriminator threshold at 0.25 PE is represented as a dotted black vertical line. For visual purposes, a vertical dashed red line is also included at 0.15 PE.

240 multiple smaller pulses, therefore it is always critical to perform a summation of the charge within  
 241 a window. The 100 ns summation also means that the pulse selection will occasionally accept MPE  
 242 events.

## 243 2.2 Characterizing the low-charge region

244 Fig. 2 (right) shows the charge distributions of the selected pulses that pass the single photoelec-  
 245 tron pulse selection for string 1, optical module 1 (DOM (1,1)). In the low-charge region (below  
 246 0.25 PE), we see a second threshold at approximately 0.13 PE. This is a software-defined threshold  
 247 that comes from a gradient-related termination condition in WaveDeform. The threshold was set to  
 248 avoid electronic noise being interpreted as PMT pulses and contaminating the low-charge region.

249 The steeply falling component of the distribution from 0.13 PE to 0.25 PE is in agreement with  
 250 the in-time laser tests mentioned in Sec. 1.1. This section will assess the noise contribution to this  
 251 region and examine the effect on the charge distribution and noise contribution by lowering the  
 252 WaveDeform threshold.

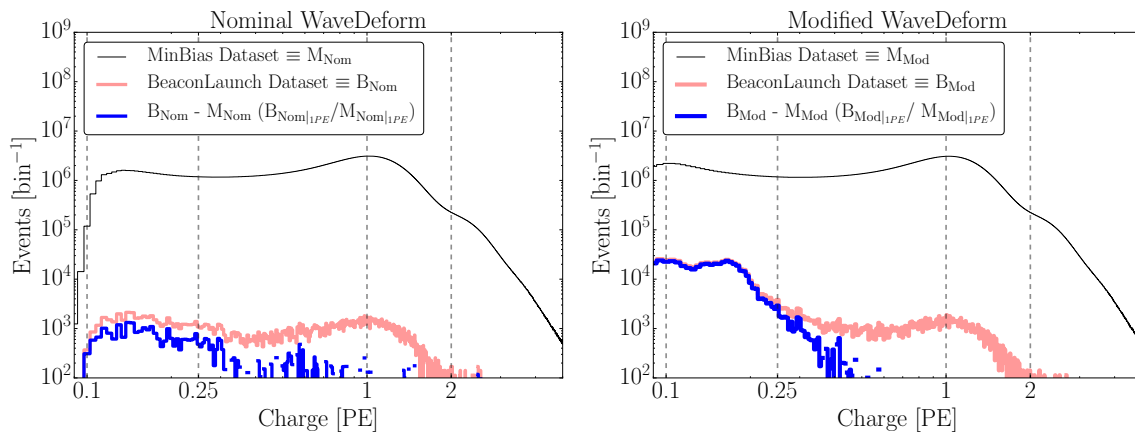


**Figure 3.** The cumulative charge distributions of all DOMs for the MinBias and BeaconLaunch datasets. The blue histogram shows the expected contribution from noise. This was found by subtracting the shape of the MinBias dataset from the BeaconLaunch dataset. Left: The charge distributions for the standard WaveDeform settings. Right: The charge distributions for the modified WaveDeform settings.

253 Fig. 3 (left) shows the charge distributions for the MinBias (black) and the BeaconLaunch  
 254 (red) datasets using the default settings of WaveDeform. As mentioned in Sec. 1.2, occasionally  
 255 a photoelectron will be coincident with the forced BeaconLaunch time window. These charges  
 256 populate a SPE distribution. Subtracting the shape of the MinBias charge distribution from the  
 257 BeaconLaunch dataset yields an estimate of the amount of electronic noise contamination (blue).  
 258 The bin with the largest signal-to-noise ratio (SNR) above 0.1 PE was found to have a SNR of  
 259 0.0013. The SNR for the full distribution was found to be 0.0005. Fig. 3 (right) shows the same  
 260 data after lowering the WaveDeform threshold. Correspondingly, the bin with the largest SNR was  
 261 found to have a SNR of 0.017, whereas the total SNR was found to be 0.0015.

262 The modified WaveDeform datasets show a minimal increase in the relative contribution of  
 263 noise to the low-charge region. From this, we can extract charge information to approximately

264 0.10 PE and improve the overall description in that region. The measured charge in this region will  
265 help constrain the values defining  $\text{Exp}_1$ .

### 266 **2.3 Fitting procedure**

267 The fit assumes that there is a negligible three-PE contribution, which is justified by the lack of  
268 statistics in the 3 PE region as well as the significant rate difference between the 1 PE and 2 PE  
269 region, as shown in Fig. 2 (right). The 2 PE charge distribution is assumed to be the SPE charge  
270 distribution convolved with itself [21]. A python-based piece of software called the "convolutional  
271 fitter" is used to determine the components of Eq. 1.1 from the measured charge distribution that  
272 includes the MPE contamination.

273 The  $\text{Exp}_2$  component, as well as the  $\text{Exp}_1$ , of Eq. 1.1 represent poorly amplified photoelec-  
274 trons, and we do not allow it to extend beyond the high-charge region of the Gaussian component.  
275 In particular, we include a constraint on the parameter  $w_2$  to ensure that it falls off with the  
276 Gaussian component:

$$w_2 < \frac{\mu + 2\sigma}{4 - \text{Ln}(N/E_2)}. \quad (2.1)$$

277 This equation was found by setting the  $\text{Exp}_2$  to be  $1/e^2$  that of the Gaussian component at two  
278 sigma (the  $\text{Exp}_1$  is neglected from this equation since it falls off in the low-charge region). Eq. 2.1  
279 is used as a constraint during the fit to the charge distributions.

280 Pulses that fall below the WaveDeform threshold and are not reconstructed contribute to an  
281 effective efficiency of the individual DOMs. This analysis assumes the same shape of the steeply  
282 falling exponential component ( $\text{Exp}_1$ ) for all DOMs in the detector to avoid large fluctuations in  
283 the individual DOM efficiencies. The modified WaveDeform data will strictly be used to determine  
284 the  $\text{Exp}_1$  component. Specifically, using the modified WaveDeform, we will background-subtract  
285 the BeaconLaunch distribution from the MinBias data, fit the resulting distribution to determine  
286 the components of Eq. 2.1, and use only the measured shape and normalization of  $\text{Exp}_1$  in all  
287 subsequent unmodified WaveDeform fits.

288 As described in Sec. 1.1, the Gaussian mean is used to determine the gain setting for each  
289 PMT. Therefore, it is particularly important that the fit quality in this region accurately describes the  
290 data. While fitting to the full charge distribution improves the overall fit agreement, the mismatch  
291 between the chosen functional form (Eq. 1.1) and a true SPE charge distribution can cause the  
292 Gaussian component to pull away from its ideal location. To compensate for this, the convolutional  
293 fitter prioritizes fitting to the data around the Gaussian mean. This is accomplished by first fitting  
294 to the full distribution to get an estimate of the Gaussian mean location. Then, the statistical  
295 uncertainty is reduced in the region  $\pm 0.15$  PE around the original estimated Gaussian mean, and  
296 the distribution is re-fitted.

297 Upon fitting the MinBias data with the predetermine values for  $\text{Exp}_1$ , the residual of each fit is  
298 calculated by measuring the percentage difference between the fit and the data. The average resid-  
299 ual will then be used as a global scaling factor for all SPE templates to account for the difference  
300 between the chosen model (Eq. 2.1) and the actual data.

301 All the DOMs with "failed fits" are not included in this article. A DOM is classified as having  
302 a failed fit if it does not pass one of the validity checks on the data requirements (e.g. number of

valid pulses) or goodness of fit. The majority of these DOMs have been removed from service (approximately 109 DOMs) and the remaining approximately 6 DOMs are known to have issues. In the IceCube MC simulation chain, these DOMs are assigned the average SPE template.

## 2.4 SPE template fit results

Using the background-subtracted modified WaveDeform dataset, the  $\text{Exp}_1$  component was determined by fitting the distribution from 0.1 PE to 3.5 PE. The result of the fit yielded  $E_1 = 6.9 \pm 1.5$  and  $w_1 = 0.032 \pm 0.002$  PE. The shape of  $\text{Exp}_1$  is then used to describe the low-PE charge region for all subsequent fits.

Using the MinBias dataset with the measured values of  $\text{Exp}_1$ , the SPE templates are extracted for every DOM, separately for each IceCube season (IC86.2011 to IC86.2016). The fit range for  $\text{Exp}_2$  and the Gaussian components is selected to be between 0.15 PE and 3.5 PE. An average fit was also performed on the cumulative charge distribution, in which all the data for a given DOM was summed together (labeled as "AVG"). The mean value and standard error of the IC86.AVG fit parameters, excluding  $\text{Exp}_1$ , for the subset of hardware differences are listed in Table 1. The average residual for all DOMs from 0 to 1 PE is shown in Fig. 4.

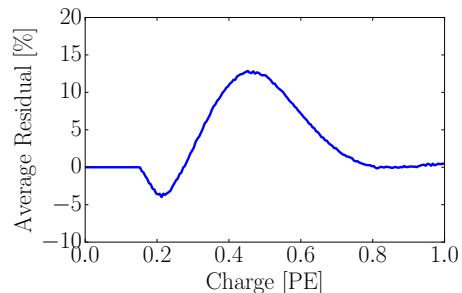


**Figure 4.** The measured average residual of the SPE templates fit.

Hardware Configuration	$\text{Exp}_2$ Amp. ( $E_2$ )	$\text{Exp}_2$ Width ( $w_2$ )	Gaus. Amp. ( $N$ )	Gaus. Mean ( $\mu$ )	Gaus. Width ( $\sigma$ )
HQE / New Toroid	$0.644 \pm 0.003$	$0.405 \pm 0.003$	$0.715 \pm 0.002$	$1.0202 \pm 0.0010$	$0.311 \pm 0.001$
NQE / New Toroids	$0.566 \pm 0.001$	$0.403 \pm 0.001$	$0.751 \pm 0.001$	$1.0238 \pm 0.0004$	$0.316 \pm 0.001$
NQE / Old Toroids	$0.525 \pm 0.002$	$0.420 \pm 0.002$	$0.813 \pm 0.002$	$1.0074 \pm 0.0007$	$0.294 \pm 0.001$

**Table 1.** The average values and standard error of each fit parameter for the subset of hardware configurations listed in the first column.

An example fit is shown in Fig. 5 for the cumulative charge distribution for DOM (1,1). The collected charge distribution is shown in the black histogram, while the convolutional fit is shown as the black line (multiplied by the residual). The extracted SPE template (also multiplied by the residual) for this DOM is shown in blue.

## 3. Discussion

### 3.1 Correlations between fit parameters and DOM hardware differences

It is evident from the data provided in Table 1 that the average shape of the SPE templates is dependent on the DOM hardware configuration. Fig. 6 shows the distribution of the measured peak-to-valley ratios and mean charge for the three different subsets of DOM hardware.

Most notably, when we examine the subset of DOMs instrumented with the new toroids, the average HQE DOM were found to have a particularly larger  $E_2$  component ( $13.8 \pm 0.6\%$ ) and

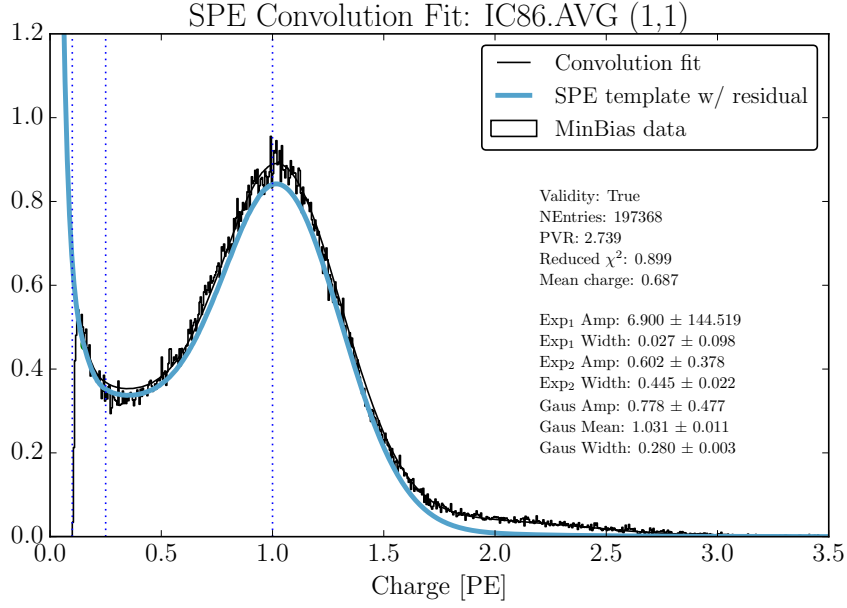


**Figure 5.** An example fit including the residual correction for DOM (1,1) using the WaveDeform dataset for seasons IC86.2011 to IC86.2016. The result from the convolutional fitter is shown as a solid black line. The extracted SPE template is shown blue.

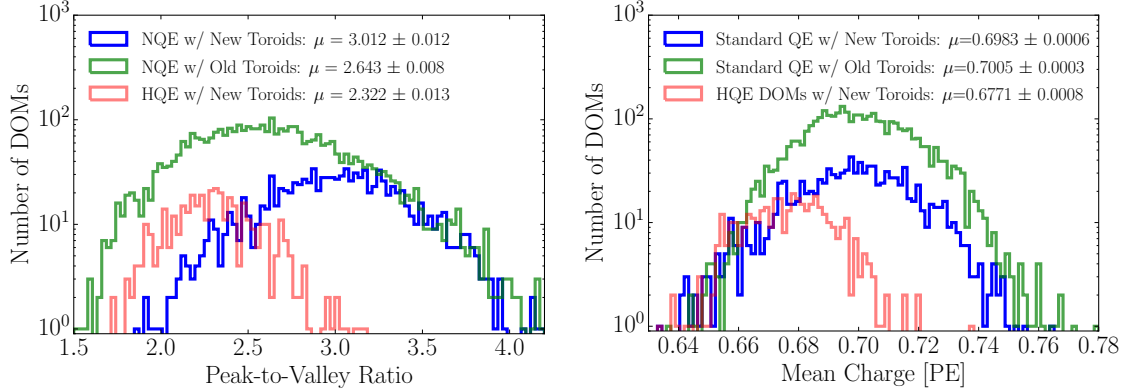


**Figure 6.** Comparison between the R7081-02MOD HQE DOMs and standard R7081-02 DOMs. Left: The peak-to-valley ratio for the two subsets of quantum efficiencies. Right: The mean charge of the individual DOM SPE templates.

335 smaller Gaussian amplitude ( $-4.77 \pm 0.03\%$ ). Consequently, the average HQE peak-to-valley ratio is measured to be  $2.322 \pm 0.013$ , corresponding to  $-12.12 \pm 0.06\%$  lower than the average  
 336 NQE DOMs. Also, interestingly, the mean charge of the average HQE DOM was found to be  
 337  $-3.34 \pm 0.01\%$  lower than for the NQE DOMs. IceCube compensates for the change in the mean  
 338 measured charge in simulation, by increasing the HQE DOM efficiency by the equivalent amount.  
 339 This ensures that the total amount of charge collected by the HQE DOMs remains the same prior  
 340 to, and after, inserting the SPE templates into simulation.

342 Similarly, using only the subset of NQE DOMs, the SPE templates comparing the method of

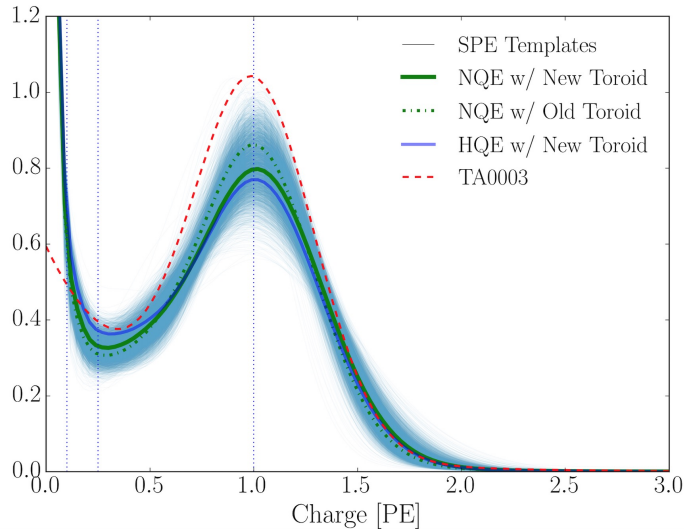


**Figure 7.** A comparison between the SPE templates (light blue band) and the TA0003 (dashed red line) distribution. The average SPE template for the Standard QE and HQE DOMs is shown as the thick blue and green lines, respectively. The SPE templates include the residual correction, and all curves are normalized.

343 AC coupling were found to have a measurably different shapes. The average Gaussian amplitude  
 344 and width for the DOMs instrumented with the old toroids were found to be  $+8.31 \pm 0.01\%$  and  $-$   
 345  $6.80 \pm 0.03\%$ , respectively. With these differences, we find a peak-to-valley ratio of  $2.643 \pm 0.008$   
 346 for the old toroid DOMs and  $3.012 \pm 0.012$  for the new toroid DOMs. The average Gaussian  
 347 mean of the fit for the DOMs with the old toroids was also found to be  $-1.6 \pm 0.1\%$  lower than  
 348 those with the new toroids. This corresponds proportionally to a change in the expected gain.  
 349 The mean charge, however, between these two hardware configurations remains very similar ( $-$   
 350  $0.346 \pm 0.001\%$ ).

351 Although the DOMs instrumented with the old toroids were deployed into the ice earlier than  
 352 those with the new toroids, the differences above is still noted when examining individual deploy-  
 353 ment years; therefore, the shape differences are not attributed to the change in the DOM behavior  
 354 over time. The DOMs with the old toroids were the first PMTs to be manufactured by Hamamatsu,  
 355 so this difference may also be attributed to a gradual change in the process parameters over the  
 356 course of PMT manufacturing, i.e. a change in the production procedure rather than the actual AC  
 357 coupling version. It is also possible that the differences originate from the transfer function that  
 358 models a single photoelectron waveform used in WaveDeform.

359 Fig. 7 illustrates the average shape differences in the measured SPE templates between the  
 360 HQE DOM with the new toroids (thick blue line), NQE with the new toroids (thick green line),  
 361 NQE with the old toroids (dash-dot green line), compared to the measured SPE templates from the  
 362 AVG charge distributions (think blue lines). The figure also shows how the TA0003 distribution  
 363 compares to this recent measurement. The shape difference in the TA0003 is attributed to better  
 364 control of the low-charge region, the difference in functional form (described in Section 1.1), and  
 365 the fact that the SPE templates sample uniformly over the entire photocathode at random incident  
 366 angles.

367 **3.2 Fitting parameters variation over time**

368 The SPE templates were extracted for each IceCube season independently to investigate the time  
 369 dependence of the fit parameters. For every DOM in the detector, the change over time of each  
 370 fit parameter (excluding  $\text{Exp}_1$ ) was calculated. Fig. 8 shows the change in a given fit parameter,  
 371 relative to the mean value, per year. The measured distribution was found to be consistent with  
 372 statistically scrambling the yearly measurements. The average of each fit parameters are found  
 373 to deviate less than 0.1%, which is in agreement with the stability checks performed in Ref. [8].  
 374 This observation holds for the individual subset of DOMs with different hardware configurations  
 375 as well.

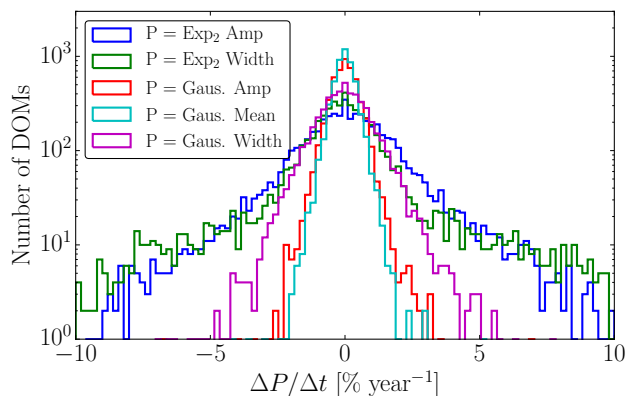


**Figure 8.** The change in the individual DOM fitted parameters over time, represented as percentage deviation from the mean fit parameter value.

376 **3.3 Quantifying observable changes when modifying the PMT charge distributions**

377 Changing the assumed gain response in simulation, as deduced from data, has different implications  
 378 depending on the typical illumination level present in different analyses. These differences are  
 379 outlined in the following discussion.

380 The PMT response is described by a combination of a "bare" efficiency,  $\eta_0$ , and a normalized  
 381 charge response function,  $f(q)$ . The bare efficiency represents the fraction of arriving photons that  
 382 result in any nonzero charge response, including those well below the discriminator threshold. The  
 383 normalization condition is:

$$\int_0^{\text{inf}} f(q) dq = 1. \quad (3.1)$$

384 Generally,  $f(q)$  and  $\eta_0$  have to be adjusted together to maintain agreement with a quantity known  
 385 from lab or in-ice measurements, such as the predicted number of pulses above threshold for a dim  
 386 source.

387 **Dim source measurements** Where light levels are low enough, sub-discriminator pulses do not  
 388 contribute any observed charge because they do not satisfy the trigger threshold, and the probability  
 389 of two photons arriving together is negligible. Given some independent way of knowing the number  
 390 of arriving photons, a lab or in-ice measurement determines the trigger fraction above threshold

391  $\eta_{0.25}$  and/or the average charge over threshold  $Q_{0.25}$ , either of which can be used to constrain the  
 392 model as follows:

$$\eta_{0.25} = \eta_0 \int_{0.25q_{pk}}^{\text{inf}} f(q) dq \quad (3.2)$$

$$Q_{0.25} = \eta_0 \int_{0.25q_{pk}}^{\text{inf}} qf(q) dq \quad (3.3)$$

393 Here, the discriminator threshold is assumed to be 0.25 times the peak position  $q_{pk}$ . It is also  
 394 useful to multiply observed charges by  $q_{pk}$ , since we set each PMT gain by such a reference, and  
 395 then a measurement constraint would be stated in terms of  $Q_{0.25}/q_{pk}$ .

396 **Semi-bright source measurements** Once the ATWD window is open, subsequent pulses are not  
 397 limited by the discriminator threshold. WaveDeform introduces a software termination condition at  
 398 0.1 PE (described at the end of Section 2.1). The average charge of an individual pulse that arrives  
 399 within the time window is:

$$Q_{0.10} = \eta_0 \int_{0.10q_{pk}}^{\text{inf}} qf(q) dq \quad (3.4)$$

400 **Bright source measurements** For light levels that are large, the trigger is satisfied regardless  
 401 of the response to individual photons, and the total charge per arriving photon therefore includes  
 402 contributions below both the discriminator and the WaveDeform thresholds:

$$Q_0 = \eta_0 \int_0^{\text{inf}} qf(q) dq \quad (3.5)$$

403 As such, the total charge is directly proportional to the average charge of the SPE template,  
 404 having a strong dependence on  $\text{Exp}_1$ .

### 405 3.3.1 Model comparison

406 When the charge distribution model is changed in a way that preserves agreement with the mea-  
 407 sured  $\eta_{0.25}$  or  $Q_{0.25}/q_{pk}$ , i.e.,  $\eta_0$  is adjusted properly for changes in  $f(q)$ , the physical effect can be  
 408 summarized by the change in the bright-to-dim ratios  $Q_0/Q_{0.25}$ , and  $Q_0/Q_{0.10}$ . Conveniently, these  
 409 ratios depend only on the shape of  $f(q)$ . Table 2 compares these ratios in terms of the TA0003  
 410 charge distribution and the SPE templates described here. It is shown that there are sub-percent  
 411 level differences in the physically-observable bright-to-dim ratios.

Model	Detector	$Q_0/Q_{0.25}$	$Q_0/Q_{0.10}$	$\eta_{0.25}/Q_{0.25}$
TA0003	All DOMs	1.017	1.0031	1.05
SPE Templates	HQE + New Toroids	$1.021 \pm 0.002$	$1.0041 \pm 0.0004$	$1.05 \pm 0.02$
	NQE + New Toroids	$1.018 \pm 0.002$	$1.0035 \pm 0.0005$	$1.03 \pm 0.02$
	NQE + Old Toroids	$1.017 \pm 0.002$	$1.0033 \pm 0.0005$	$1.05 \pm 0.02$

**Table 2.** The distribution in bright-to-dim ratios for the previous charge distribution (TA0003) and the individual DOM SPE templates for the IceCube and DeepCore detectors.

412 **3.4 SPE templates in simulation**

413 The IceCube Monte Carlo simulation chain assigns a charge to every photoelectron generated at  
 414 the surface of the photocathode. The charge is determined by sampling from a normalized charge  
 415 distribution probability density function. A comparison between describing the charge distribution  
 416 using the SPE templates and the TA0003 distribution follows.

417 Two simulation sets consisting of the same events were processed through the IceCube Monte  
 418 Carlo simulation chain to the final analysis level of an update to the IC86.2011 sterile neutrino  
 419 analysis [22]. Here, the events that pass the cuts are >99.9% pure upgoing (a trajectory ori-  
 420 ented upwards relative to the horizon) secondary muons produced by charged current muon neu-  
 421 trino/antineutrino interactions. The muon energy range of this event selection is between approxi-  
 422 mately 500 GeV and 10 TeV.

423 Fig. 9 (left) shows the distribution of the total measured charge in a single DOM during each  
 424 event. The data is shown for the full IC86.2012 season but is statistically equivalent to any of the  
 425 other seasons. The simulation set using the TA0003 charge distribution is shown in orange, and that  
 426 using the SPE templates is shown in blue. The bottom of the plot shows the ratio of the measured  
 427 quantity relative to data. Fig. 9 (right) shows the distribution of the measured total charge on a  
 428 DOM (after noise removal) divided by the number of channels, or DOMs, that participated in the  
 429 event. Both plots in Fig. 9 have been normalized such that the area under the histograms is the  
 430 same.

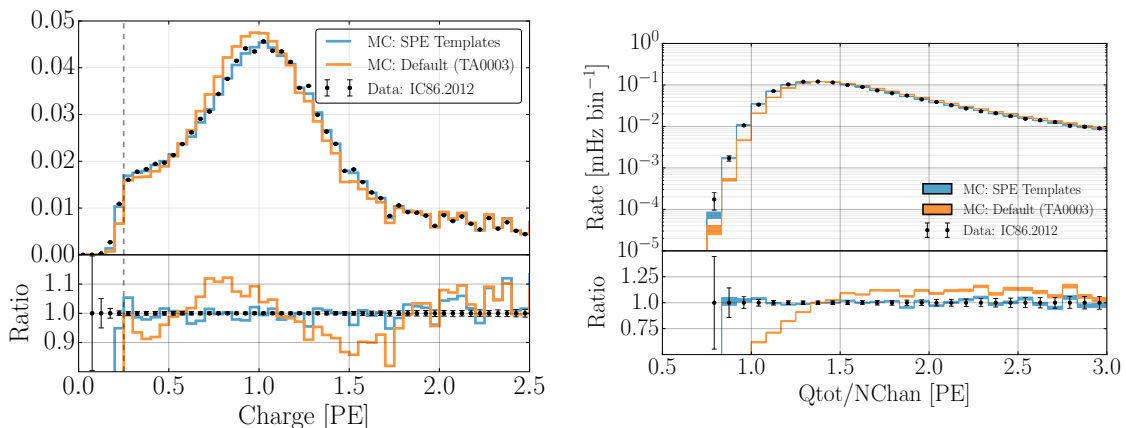


**Figure 9.** A comparison between the SPE templates (blue) and the TA0003 (orange) model for describing the SPE charge distribution in Monte Carlo. The simulation is compared to the 2012 IceCube season. Left: The total measured charge per DOM, per event at analysis level. Right: The distribution of the total measured charge of an event divided by the number of DOMs that participated in the event.

431 The SPE templates clearly improve the overall MC description of these two variables. IceCube  
 432 includes a systematic uncertainty in all analyses, which scales the DOM efficiency to account for  
 433 effects that change the total observed charge. This systematic compensates for the overall mean  
 434 charge shift introduced using the SPE templates; however, the SPE templates now introduce DOM-  
 435 to-DOM differences. This is not expected to change the IceCube physics results since analyses are  
 436 sensitive to the overall detector performance rather than the individual DOM variations.

### 437 **3.5 SPE templates for calibration**

438 The gain setting on each DOM is calibrated at the beginning of the season such that the Gaussian  
439 mean charge distribution corresponds to a gain of  $10^7$ , or equivalently 1 PE. Since the method used  
440 to extract the Gaussian mean described in this article is different from the previous method used  
441 for calibration of the DOMs, the total measured charge from a DOM is expected to change with  
442 the updated calibration.

443 The Gaussian mean component of the fit of every year is found to be on average  $2.00 \pm 0.03\%$   
444 higher than unity with a standard deviation of 3.54%, corresponding to a systematic overestimation  
445 of the measured charge in the detector. This correction to the measured charge can be implemented  
446 retroactively by dividing the reported charge from WaveDeform by the corresponding Gaussian  
447 mean for a given DOM. Alternatively, the MC can account for this difference by simply inserting  
448 the SPE templates with Gaussian mean matching the values found in the data. Both of these  
449 solutions will be used in future IceCube data/MC production.

## 450 **4. Conclusion**

451 This article outlines the procedure used for collecting a relatively pure sample of single photoelec-  
452 tron charges for each of the in-ice DOMs in IceCube. MPE contamination was removed under  
453 the assumption that it is the convolution of the SPE distribution from multiple times. The SPE  
454 templates were extracted for each DOM and each season in the IceCube and DeepCore detectors  
455 and investigated for correlations with hardware-related features. Neither detector shows more than  
456 a 0.1% deviation in any of the fitted parameters over the investigated seasons, in agreement with  
457 Ref. [8]. Yearly variations in the fit parameters are consistent with statistical fluctuations. The  
458 HQE DOMs were found to have a smaller peak-to-valley ratio than the NQE DOMs, as well as  
459 an overall  $-3.34 \pm 0.01\%$  lower mean charge. Similarly, DOMs instrumented with the old toroids  
460 were found to have a narrower and larger Gaussian component. The origin of this difference is still  
461 under investigation.

462 The SPE templates were implemented into the MC simulation production chain and the results  
463 were compared to the default charge distribution (TA0003). A significant improvement in the  
464 description of the low-level variables, total charge per DOM, and total charge per event over the  
465 number of channels was shown. IceCube includes a systematic that scales the bare efficiency of  
466 the DOMs to maintain agreement with a quantity known from lab or in-ice measurements. After  
467 accounting for this shift, the effect on physics analysis, as shown by the bright-to-dim ratios, is  
468 expected to percent level changes in the measured charge.

469 The new method for extracting the calibration constant that determines the gain setting on each  
470 of the PMTs (the Gaussian mean of the fit) has been revised and shows that the average gain was  
471  $2.00 \pm 0.03\%$  larger than expected. This will be accounted for in future IceCube data reprocessing  
472 and simulation.

## 474 **Acknowledgments**

475 We acknowledge the support from the following agencies: U.S. National Science Foundation - Of-

476 fice of Polar Programs, U.S. National Science Foundation - Physics Division, University of Wiscon-  
477 sin Alumni Research Foundation, the Grid Laboratory Of Wisconsin (GLOW) grid infrastructure  
478 at the University of Wisconsin - Madison, the Open Science Grid (OSG) grid infrastructure; U.S.  
479 Department of Energy, and National Energy Research Scientific Computing Center, the Louisiana  
480 Optical Network Initiative (LONI) grid computing resources; Natural Sciences and Engineering  
481 Research Council of Canada, WestGrid and Compute/Calcul Canada; Swedish Research Coun-  
482 cil, Swedish Polar Research Secretariat, Swedish National Infrastructure for Computing (SNIC),  
483 and Knut and Alice Wallenberg Foundation, Sweden; German Ministry for Education and Re-  
484 search (BMBF), Deutsche Forschungsgemeinschaft (DFG), Helmholtz Alliance for Astroparticle  
485 Physics (HAP), Research Department of Plasmas with Complex Interactions (Bochum), Germany;  
486 Fund for Scientific Research (FNRS-FWO), FWO Odysseus programme, Flanders Institute to en-  
487 courage scientific and technological research in industry (IWT), Belgian Federal Science Policy  
488 Office (Belspo); University of Oxford, United Kingdom; Marsden Fund, New Zealand; Australian  
489 Research Council; Japan Society for Promotion of Science (JSPS); the Swiss National Science  
490 Foundation (SNSF), Switzerland; National Research Foundation of Korea (NRF); Villum Fonden,  
491 Danish National Research Foundation (DNRF), Denmark.

492 **References**

- 493 [1] J. Ahrens *et al.*, “Icecube preliminary design document,” URL: <http://www.icecube.wisc.edu/science/publications/pdd>, 2001.  
494
- 495 [2] A. Achterberg, M. Ackermann, J. Adams, J. Ahrens, K. Andeen, D. Atlee, J. Baccus, J. Bahcall,  
496 X. Bai, B. Baret, *et al.*, “First year performance of the icecube neutrino telescope,” *Astroparticle*  
497 *Physics*, vol. 26, no. 3, pp. 155–173, 2006.
- 498 [3] I. Collaboration *et al.*, “Evidence for high-energy extraterrestrial neutrinos at the icecube detector,”  
499 *Science*, vol. 342, no. 6161, p. 1242856, 2013.
- 500 [4] R. Abbasi, Y. Abdou, T. Abu-Zayyad, M. Ackermann, J. Adams, J. Aguilar, M. Ahlers, M. Allen,  
501 D. Altmann, K. Andeen, *et al.*, “The design and performance of icecube deepcore,” *Astroparticle*  
502 *physics*, vol. 35, no. 10, pp. 615–624, 2012.
- 503 [5] R. Abbasi, M. Ackermann, J. Adams, M. Ahlers, J. Ahrens, K. Andeen, J. Auffenberg, X. Bai,  
504 M. Baker, S. Barwick, *et al.*, “The icecube data acquisition system: Signal capture, digitization, and  
505 timestamping,” *Nuclear Instruments and Methods in Physics Research Section A: Accelerators,*  
506 *Spectrometers, Detectors and Associated Equipment*, vol. 601, no. 3, pp. 294–316, 2009.
- 507 [6] R. Abbasi, Y. Abdou, T. Abu-Zayyad, J. Adams, J. Aguilar, M. Ahlers, K. Andeen, J. Auffenberg,  
508 X. Bai, M. Baker, *et al.*, “Calibration and characterization of the icecube photomultiplier tube,”  
509 *Nuclear Instruments and Methods in Physics Research Section A: Accelerators, Spectrometers,*  
510 *Detectors and Associated Equipment*, vol. 618, no. 1-3, pp. 139–152, 2010.
- 511 [7] Hamamatsu, “Datasheet,” URL: <https://www.hamamatsu.com/>, 2018.
- 512 [8] M. Aartsen *et al.*, “The icecube neutrino observatory: Instrumentation and online systems, jinst 12  
513 (03)(2017) p03012,” *arXiv preprint arXiv:1612.05093*, pp. 1748–0221.
- 514 [9] R. Stokstad, “Design and performance of the icecube electronics,” 2005.
- 515 [10] Hamamatsu, “Resources: Basics and applications,” URL:  
516 [https://www.hamamatsu.com/resources/pdf/etd/PMT\\_handbook\\_v3aE.pdf](https://www.hamamatsu.com/resources/pdf/etd/PMT_handbook_v3aE.pdf), 2018.
- 517 [11] Hamamatsu, “Handbook resources, chapter 4,” URL:  
518 [https://www.hamamatsu.com/resources/pdf/etd/PMT\\_handbook\\_v3aE-Chapter4.pdf](https://www.hamamatsu.com/resources/pdf/etd/PMT_handbook_v3aE-Chapter4.pdf), 2018.
- 519 [12] J. Brack, B. Delgado, J. Dhooghe, J. Felde, B. Gookin, S. Grullon, J. Klein, R. Knapik, A. LaTorre,  
520 S. Seibert, *et al.*, “Characterization of the hamamatsu r11780 12 in. photomultiplier tube,” *Nuclear*  
521 *Instruments and Methods in Physics Research Section A: Accelerators, Spectrometers, Detectors and*  
522 *Associated Equipment*, vol. 712, pp. 162–173, 2013.
- 523 [13] E. Calvo, M. Cerrada, C. Fernández-Bedoya, I. Gil-Botella, C. Palomares, I. Rodríguez, F. Toral, and  
524 A. Verdugo, “Characterization of large-area photomultipliers under low magnetic fields: Design and  
525 performance of the magnetic shielding for the double chooz neutrino experiment,” *Nuclear*  
526 *Instruments and Methods in Physics Research Section A: Accelerators, Spectrometers, Detectors and*  
527 *Associated Equipment*, vol. 621, no. 1-3, pp. 222–230, 2010.
- 528 [14] F. Kaether and C. Langbrandtner, “Transit time and charge correlations of single photoelectron events  
529 in r7081 photomultiplier tubes,” *Journal of Instrumentation*, vol. 7, no. 09, p. P09002, 2012.
- 530 [15] B. Lubsandorzhev, P. Pokhil, R. Vasiljev, and A. Wright, “Studies of prepulses and late pulses in the  
531 8" electron tubes series of photomultipliers,” *Nuclear Instruments and Methods in Physics Research*  
532 *Section A: Accelerators, Spectrometers, Detectors and Associated Equipment*, vol. 442, no. 1-3,  
533 pp. 452–458, 2000.

- 534 [16] K. Ma, W. Kang, J. Ahn, S. Choi, Y. Choi, M. Hwang, J. Jang, E. Jeon, K. Joo, H. Kim, *et al.*, “Time  
535 and amplitude of afterpulse measured with a large size photomultiplier tube,” *Nuclear Instruments  
536 and Methods in Physics Research Section A: Accelerators, Spectrometers, Detectors and Associated  
537 Equipment*, vol. 629, no. 1, pp. 93–100, 2011.
- 538 [17] S. Torre, T. Antonioli, and P. Benetti, “Study of afterpulse effects in photomultipliers,” *Review of  
539 scientific instruments*, vol. 54, no. 12, pp. 1777–1780, 1983.
- 540 [18] M. Aartsen, K. Abraham, M. Ackermann, J. Adams, J. Aguilar, M. Ahlers, M. Ahrens, D. Altmann,  
541 T. Anderson, M. Archinger, *et al.*, “Characterization of the atmospheric muon flux in icecube,”  
542 *Astroparticle physics*, vol. 78, pp. 1–27, 2016.
- 543 [19] M. Aartsen, R. Abbasi, Y. Abdou, M. Ackermann, J. Adams, J. Aguilar, M. Ahlers, D. Altmann,  
544 J. Auffenberg, X. Bai, *et al.*, “Measurement of south pole ice transparency with the icecube led  
545 calibration system,” *Nuclear Instruments and Methods in Physics Research Section A: Accelerators,  
546 Spectrometers, Detectors and Associated Equipment*, vol. 711, pp. 73–89, 2013.
- 547 [20] M. Aartsen, R. Abbasi, M. Ackermann, J. Adams, J. Aguilar, M. Ahlers, D. Altmann, C. Arguelles,  
548 J. Auffenberg, X. Bai, *et al.*, “Energy reconstruction methods in the icecube neutrino telescope,”  
549 *Journal of Instrumentation*, vol. 9, no. 03, p. P03009, 2014.
- 550 [21] R. Dossi, A. Ianni, G. Ranucci, and O. J. Smirnov, “Methods for precise photoelectron counting with  
551 photomultipliers,” *Nuclear Instruments and Methods in Physics Research Section A: Accelerators,  
552 Spectrometers, Detectors and Associated Equipment*, vol. 451, no. 3, pp. 623–637, 2000.
- 553 [22] M. Aartsen, K. Abraham, M. Ackermann, J. Adams, J. Aguilar, M. Ahlers, M. Ahrens, D. Altmann,  
554 K. Andeen, T. Anderson, *et al.*, “Searches for sterile neutrinos with the icecube detector,” *Physical  
555 review letters*, vol. 117, no. 7, p. 071801, 2016.